A&A 649, A88 (2021)
https://doi.org/10.1051/0004-6361/202039805

Astronomy & Astrophysics

KiDS-1000 Cosmology: Constraints beyond flat ΛCDM

Tilman Tröster[1], Marika Asgari[1], Chris Blake[2], Matteo Cataneo[1], Catherine Heymans[1,3], Hendrik Hildebrandt[3], Benjamin Joachimi[4], Chieh-An Lin (林皆安)[1], Ariel G. Sánchez[5], Angus H. Wright[3], Maciej Bilicki[6], Benjamin Bose[7], Martin Crocce[8,9], Andrej Dvornik[3], Thomas Erben[10], Benjamin Giblin[1], Karl Glazebrook[2], Henk Hoekstra[11], Shahab Joudaki[12], Arun Kannawadi[13], Fabian Köhlinger[3], Konrad Kuijken[11], Chris Lidman[14,15], Lucas Lombriser[7], Alexander Mead[16], David Parkinson[17], HuanYuan Shan (陕欢源)[18,19], Christian Wolf[14,15], and Qianli Xia (夏千里)[1]

[1] Institute for Astronomy, University of Edinburgh, Royal Observatory, Blackford Hill, Edinburgh EH9 3HJ, UK
e-mail: ttr@roe.ac.uk
[2] Centre for Astrophysics & Supercomputing, Swinburne University of Technology, PO Box 218, Hawthorn, VIC 3122, Australia
[3] Ruhr-Universität Bochum, Astronomisches Institut, German Centre for Cosmological Lensing (GCCL), Universitätsstr. 150, 44801 Bochum, Germany
[4] Department of Physics and Astronomy, University College London, Gower Street, London WC1E 6BT, UK
[5] Max-Planck-Institut für Extraterrestrische Physik, Postfach 1312, Giessenbachstrasse 1, 85741 Garching, Germany
[6] Center for Theoretical Physics, Polish Academy of Sciences, Al. Lotników 32/46, 02-668 Warsaw, Poland
[7] Département de Physique Théorique, Université de Genève, 24 Quai Ernest Ansermet, 1211 Genève 4, Switzerland
[8] Institute of Space Sciences (ICE, CSIC), Campus UAB, Carrer de Can Magrans, s/n, 08193 Barcelona, Spain
[9] Institut d'Estudis Espacials de Catalunya (IEEC), Carrer Gran Capita 2, 08034 Barcelona, Spain
[10] Argelander-Institut für Astronomie, Universität Bonn, Auf dem Hügel 71, 53121 Bonn, Germany
[11] Leiden Observatory, Leiden University, Niels Bohrweg 2, 2333 CA Leiden, The Netherlands
[12] Department of Physics, University of Oxford, Denys Wilkinson Building, Keble Road, Oxford OX1 3RH, UK
[13] Department of Astrophysical Sciences, Princeton University, 4 Ivy Lane, Princeton, NJ 08544, USA
[14] Centre for Gravitational Astrophysics, College of Science, Australian National University, Acton, ACT 2601, Australia
[15] Research School of Astronomy and Astrophysics, Australian National University, Canberra, ACT 2600, Australia
[16] Institut de Ciències del Cosmos, Universitat de Barcelona, Martí Franquès 1, 08028 Barcelona, Spain
[17] Korea Astronomy and Space Science Institute, 776 Daedeokdae-ro, Yuseong-gu, Daejeon 34055, Republic of Korea
[18] Shanghai Astronomical Observatory (SHAO), Nandan Road 80, Shanghai 200030, PR China
[19] University of Chinese Academy of Sciences, Beijing 100049, PR China

Received 30 October 2020 / Accepted 17 February 2021

ABSTRACT

We present constraints on extensions to the standard cosmological model of a spatially flat Universe governed by general relativity, a cosmological constant (Λ), and cold dark matter (CDM) by varying the spatial curvature Ω_K, the sum of the neutrino masses $\sum m_\nu$, the dark energy equation of state parameter w, and the Hu-Sawicki $f(R)$ gravity f_{R0} parameter. With the combined 3×2 pt measurements of cosmic shear from the Kilo-Degree Survey (KiDS-1000), galaxy clustering from the Baryon Oscillation Spectroscopic Survey (BOSS), and galaxy-galaxy lensing from the overlap between KiDS-1000, BOSS, and the spectroscopic 2-degree Field Lensing Survey, we find results that are fully consistent with a flat ΛCDM model with $\Omega_K = 0.011^{+0.054}_{-0.057}$, $\sum m_\nu < 1.76\,\mathrm{eV}$ (95% CL), and $w = -0.99^{+0.11}_{-0.13}$. The f_{R0} parameter is unconstrained in our fully non-linear $f(R)$ cosmic shear analysis. Considering three different model selection criteria, we find no clear preference for either the fiducial flat ΛCDM model or any of the considered extensions. In addition to extensions to the flat ΛCDM parameter space, we also explore restrictions to common subsets of the flat ΛCDM parameter space by fixing the amplitude of the primordial power spectrum to the *Planck* best-fit value, as well as adding external data from supernovae and lensing of the cosmic microwave background (CMB). Neither the beyond-ΛCDM models nor the imposed restrictions explored in this analysis are able to resolve the $\sim3\sigma$ tension in S_8 between the 3×2 pt constraints and the *Planck* temperature and polarisation data, with the exception of wCDM, where the S_8 tension is resolved. The tension in the wCDM case persists, however, when considering the joint S_8–w parameter space. The joint flat ΛCDM CMB lensing and 3×2 pt analysis is found to yield tight constraints on $\Omega_\mathrm{m} = 0.307^{+0.008}_{-0.013}$, $\sigma_8 = 0.769^{+0.022}_{-0.010}$, and $S_8 = 0.779^{+0.013}_{-0.013}$.

Key words. cosmology: observations – cosmological parameters – gravitational lensing: weak – large-scale structure of Universe – dark energy – methods: statistical

1. Introduction

A wide range of cosmological observations support a theoretical model for the Universe comprised of cold dark matter (CDM) and a cosmological constant (Λ), with baryons very much in the minority. These components are connected through a spatially flat gravitational framework within general relativity. This flat ΛCDM model can independently describe the temperature fluctuations in the cosmic microwave background (CMB, Planck Collaboration VI 2020), the baryon acoustic oscillation and redshift-space distortions in the clustering of galaxies (BAO and RSD, Alam et al. 2017; eBOSS Collaboration 2021), the accelerating expansion rate seen in the distance-redshift relation of Type Ia supernovae (SNe, Scolnic et al. 2018), the

present-day expansion rate as measured using a distance ladder calibrated through Cepheid variables (Riess et al. 2019) or strongly lensed quasars (Wong et al. 2020), and the weak gravitational lensing of background light by foreground large-scales structures (Troxel et al. 2018; Hamana et al. 2020; Asgari et al. 2021; Planck Collaboration VIII 2020).

The flat ΛCDM model is highly successful in describing these observables independently, but differences arise in the precise values of some cosmological components when analysing certain probes in combination. In comparison to values predicted from the best-fitting flat ΛCDM model to observations of the CMB (Planck Collaboration VI 2020), Riess et al. (2019), and Wong et al. (2020) report ∼4−5σ differences in direct local measurements of the Hubble parameter H_0, with other measurements, such as the inverse distance ladder (eBOSS Collaboration 2021) or the tip of the red giant branch (Freedman et al. 2020), lying in between. Asgari et al. (2021) report ∼3σ differences in $S_8 = \sigma_8 \sqrt{\Omega_m/0.3}$, which is a direct measure of the clustering and density of large-scale structures, following the trend to lower S_8 values seen in other weak gravitational lensing surveys (e.g. Heymans et al. 2013; Troxel et al. 2018; Hikage et al. 2019). Provided that all sources of systematic uncertainty have been accounted for in each analysis, the tensions reported between early and late-time probes of the Universe can be considered as potential evidence for the existence of additional components in our cosmological model, beyond flat ΛCDM.

Such extensions have been considered before (e.g. Planck Collaboration XIV 2016; Joudaki et al. 2017a; Dark Energy Survey Collaboration 2019; Planck Collaboration VI 2020; eBOSS Collaboration 2021; Dhawan et al. 2020), with no strong evidence for a Universe that deviates from flat ΛCDM with a minimal neutrino mass. While the combination of CMB and large-scale structure data rules out strong deviations from a flat ΛCDM model, the constraints from just the early or late-time Universe are much weaker, with *Planck* data favouring a closed Universe (e.g. Planck Collaboration VI 2020; Ooba et al. 2018; Park & Ratra 2019; Handley 2021; Di Valentino et al. 2020) but see also Efstathiou & Gratton (2020) for a different view.

Here we explore extensions to the flat ΛCDM model independently of CMB temperature and polarisation data, presenting constraints on the cosmological parameters that describe four separate additions. We allow for non-zero curvature (oΛCDM), include uncertainty in the sum of the neutrino masses (νΛCDM), replace the cosmological constant with an evolving dark energy component (wCDM), and explore modifications to standard gravity using the Hu & Sawicki (2007) $f(R)$-gravity model, where the gravitational force is enhanced in low-density regions.

To confront this range of models, we compare CMB temperature and polarisation observations[1] from Planck Collaboration VI (2020) to different combinations of late Universe probes. We analyse the weak gravitational lensing of galaxies, imaged by the fourth data release of the Kilo-Degree Survey (KiDS-1000, Kuijken et al. 2019), the gravitational lensing of the CMB (Planck Collaboration VIII 2020), Type Ia SNe (Scolnic et al. 2018), and galaxy clustering observations from the twelfth data release of the Baryon Oscillation Spectroscopic Survey (Alam et al. 2017).

In Sect. 2, we summarise the cosmological observations that we analyse in this paper, as well as the methodology. We introduce the ΛCDM extensions that we adopt in Sect. 3 and present our model constraints in Sect. 4. We conclude our analysis in Sect. 5. In the appendices we demonstrate that our constraints on S_8 are insensitive to two potential sources of systematic error in our analysis. In Appendix A we compare parameter constraints using two different models to account for our uncertainty on how baryon feedback impacts the shape of the non-linear matter power spectrum. In Appendix B we exclude large-scale information from the galaxy clustering observable and introduce informative priors on the tilt of the primordial power spectrum, n_s.

[1] Unless otherwise specified, '*Planck* data' shall refer to the primary anisotropy data of the Planck Collaboration VI (2020) TTTEEE+lowE likelihood.

2. Data and methodology

The data and methodology, unless mentioned otherwise, match those presented by Heymans et al. (2021). Here we summarise the salient points and refer the reader to Joachimi et al. (2021) for details about the methodology, Asgari et al. (2021) for the cosmic shear analysis, and Heymans et al. (2021) for an in-depth description of the multi-probe analysis of KiDS, BOSS, and 2-degree Field Lensing Survey (2dFLenS). .

2.1. KiDS, BOSS, and 2dFLenS data

The fourth data release of the Kilo-Degree Survey images 1006 deg^2 in nine bands, spanning the optical to the near-infrared (Kuijken et al. 2019). The survey strategy is optimised for weak lensing observations with accuracy and precision in the shear and redshift estimates aided by high-resolution deep imaging in the r-band, a camera with a smoothly varying and low-ellipticity point-spread function, complete matched-depth observations across the full wavelength range (Wright et al. 2019), and auxiliary imaging of deep spectroscopic calibration fields. Giblin et al. (2021) present the KiDS-1000 weak lensing shear catalogue, along with a series of null tests to quantify any systematic signals associated with the instrument, verifying that they do not introduce any bias in a cosmological analysis. Hildebrandt et al. (2021) present the KiDS-1000 photometric redshift estimates for the 'gold' galaxy sample, selected to ensure complete representation in the spectroscopic calibration sample (Wright et al. 2020). The resulting redshift distributions are validated using measurements of galaxy clustering between spectroscopic and photometric samples (van den Busch et al. 2020; Hildebrandt et al. 2021).

The Baryon Oscillation Spectroscopic Survey (BOSS, Dawson et al. 2013) of a sample of 1.2 million luminous red galaxies (LRGs) over an effective area of 9329 deg^2 provides the optimal data set to observe large-scale galaxy clustering at high signal-to-noise out to redshift $z < 0.75$. Alam et al. (2017) present a compilation of different statistical analyses of the baryon acoustic oscillation peak and the redshift-space distortions of the twelfth data release (DR12) of the BOSS sample. Combined with CMB observations from Planck Collaboration XIII (2016), Alam et al. (2017) set constraints on oΛCDM, wCDM, and νΛCDM cosmological models, with the joint data set showing no preference for extending the cosmological model beyond flat ΛCDM. The same conclusion is drawn, with improved precision, in the recent eBOSS Collaboration (2021) galaxy clustering analysis. This extended-BOSS survey includes galaxy and quasar samples out to $z < 2.2$, and Lyman-α forest observations between $2 < z < 3.5$.

The 'galaxy-galaxy lensing' (GGL) of background KiDS galaxies by foreground LRGs is measured on the overlapping areas of KiDS with BOSS DR12 and 2dFLenS (Blake et al. 2016). 2dFLenS covers 731 deg^2, with spectroscopic redshifts

for 70 000 galaxies out to $z < 0.9$ and was designed to target areas already mapped by weak lensing surveys to facilitate 'same-sky' lensing-clustering analyses (Johnson et al. 2017; Amon et al. 2018; Joudaki et al. 2018; Blake et al. 2020).

Cosmological constraints on the parameters of the flat ΛCDM analysis of KiDS-1000 are presented in Asgari et al. (2021) and Heymans et al. (2021). Asgari et al. (2021) analyse the observed evolution of weak lensing by large-scale structures, referred to as cosmic shear, in five redshift bins, using a range of different two-point statistics. Heymans et al. (2021) combine these cosmic shear measurements with BOSS DR12 galaxy clustering observations from Sánchez et al. (2017) and GGL observations of KiDS-1000 galaxies by LRGs from BOSS and 2dFLenS. The combination of these three two-point large-scale structure probes is often referred to as '3×2 pt', with the methodology described and validated using a large suite of mock survey catalogues in Joachimi et al. (2021).

We choose angular power spectrum estimates for our cosmic shear and GGL summary statistics, following Heymans et al. (2021). Specifically, we use the 'band power' estimator, a linear transformation of the real-space two-point correlation functions (Schneider et al. 2002), and estimate the angular shear and GGL power spectra in eight logarithmically spaced bands between $\ell = 100$ and $\ell = 1500$, for five tomographic redshift bins between $z = 0.1$ and $z = 1.2$, and the two spectroscopic lens bins $z \in (0.2, 0.5]$ and $z \in (0.5, 0.75]$. We discard GGL measurements at small scales and where there is overlap between the source and lens bins due to limitations in our modelling of non-linear galaxy bias and intrinsic alignment.

Our galaxy clustering measurements are adopted from Sánchez et al. (2017), who analyse the clustering of BOSS galaxies using the anisotropic galaxy correlation function divided into 'wedges'. We use the two non-overlapping redshift bins of the combined galaxy sample of Alam et al. (2017), including galaxy separations between $20\,h^{-1}$ Mpc and $160\,h^{-1}$ Mpc. In a re-analysis of this data set, Tröster et al. (2020) demonstrate that constraints on the flat ΛCDM model from BOSS clustering alone are fully consistent with *Planck*, but have a preference for lower values of the clustering parameter S_8. This result is confirmed in two independent BOSS-only re-analyses of the Beutler et al. (2017) Fourier-space BOSS clustering measurements (Ivanov et al. 2020; d'Amico et al. 2020). It is therefore relevant to combine BOSS galaxy clustering constraints with cosmological probes alternative to the CMB, to explore joint constraints on extensions to the flat ΛCDM model.

2.2. Likelihood and inference setup

Our inference pipeline is based on a modified version of COSMOSIS[2] (Zuntz et al. 2015), which we call KCAP[3]. Parameter sampling is performed using MULTINEST (Feroz & Hobson 2008; Feroz et al. 2009, 2019), using 500 or 1000 live points, and an efficiency parameter of 0.3. The sampled parameters and priors are summarised in Table 1. We vary 12 parameters in our fiducial cosmic shear analysis, 13 parameters for the galaxy clustering analysis, and 20 parameters in our 3×2 pt analysis.

[2] https://bitbucket.org/joezuntz/cosmosis
[3] https://github.com/KiDS-WL/kcap

Table 1. Sampled parameters and priors.

Parameter	Symbol	Prior
Hubble constant	h	[0.64, 0.82]
Baryon density	ω_b	[0.019, 0.026]
CDM density	ω_c	[0.051, 0.255]
Density fluctuation amp.	S_8	[0.1, 1.3]
Scalar spectral index	n_s	[0.84, 1.1]
Linear galaxy bias (2)	b_1	[0.5, 9]
Quadratic galaxy bias (2)	b_2	[−4, 8]
Non-local galaxy bias (2)	γ_3^-	[−8, 8]
Virial velocity parameter (2)	a_vir	[0, 12]
Intrinsic alignment amp.	A_IA	[−6, 6]
Baryon feedback amp.	A_bary	[2, 3.13]
Redshift offsets (5)	$\boldsymbol{\delta}_z$	$\mathcal{N}(\boldsymbol{\mu}; C_{\delta_z})$
SNe absolute calibration	M	[−22, −18]
Curvature	Ω_K	[−0.4, 0.4]
Sum of masses of neutrinos	$\sum m_\nu$	[0, 3.0] eV
Dark energy e.o.s. parameter	w	[−3, −0.33]
$f(R)$-gravity parameter	$\log_{10}\lvert f_{R0}\rvert$	[−8, −2]
AGN feedback strength	$\log_{10}\left(\frac{T_\mathrm{AGN}}{\mathrm{K}}\right)$	[7.3, 8.3]

Notes. Uniform priors are denoted with square brackets. The first section lists the primary cosmological parameters, while the second section lists the astrophysical and observational nuisance parameters to model galaxy bias, intrinsic galaxy alignments, baryon feedback, uncertainties in the redshift calibration, and the absolute calibration of SNe. The number of separate parameters for each redshift bin is indicated in parentheses. The redshift offset parameters are drawn from a multivariate Gaussian prior with mean $\boldsymbol{\mu}$ and covariance C_{δ_z}. The last section lists the priors for the extended parameterisations considered in this work, only one of which is varied at a time. Not all parameters are sampled in all analyses. For example, cosmic shear-only results do not vary the galaxy bias parameters.

The linear matter power spectrum and background quantities are calculated using CAMB[4] (Lewis et al. 2000), with the non-linear matter power spectrum modelled using HMCODE (Mead et al. 2016). The reaction of the non-linear matter power spectrum in the presence of $f(R)$ gravity is modelled using REACT (Bose et al. 2020). The clustering of galaxies uses the same renormalised perturbation theory model employed in Sánchez et al. (2017), while the non-linear bias for GGL uses the interpolation scheme described in Joachimi et al. (2021), Heymans et al. (2021).

The covariance of the cosmic shear and GGL data is computed based on the analytical model described in Joachimi et al. (2021). The galaxy clustering covariance is estimated from 2048 mock data realisations (Kitaura et al. 2016), accounting for effect of noise in the covariance on the bias in the inverse Wishart distribution (Kaufman 1967; Hartlap et al. 2007). As the cross-covariance between our lensing measurements (cosmic shear and GGL) and galaxy clustering is negligible (Joachimi et al. 2021), we treat the lensing and galaxy clustering data vectors as independent.

The maximum of the posterior (MAP) is estimated using the optimisation algorithm of Nelder & Mead (1965), using the 18 samples from the posterior with the highest posterior values as starting points. For likelihoods that include the galaxy clustering likelihood, we quote the weighted median of the different MAP runs as the location of the MAP, since numerical noise in

[4] https://github.com/cmbant/CAMB

the likelihood surface causes poor convergence of the posterior optimisation algorithm (Heymans et al. 2021).

2.3. Model selection

As we consider different models to describe our data, we wish to quantify which of these models describe the data best. To this end we make use of three different model selection criteria. The individual criteria differ in their dependence on point estimates, priors, and model dimensionalities. Considering a range of model selection criteria should therefore lead to a more robust quantification of whether the data prefer one model over another.

The first criterion is the deviance information criterion (DIC, Spiegelhalter et al. 2002, for applications in astronomy and cosmology see, for example, Kunz et al. 2006; Liddle 2007; Trotta 2008):

$$\mathrm{DIC} = -2\ln\mathcal{L}(\boldsymbol{\theta}_p) + 2p_{\mathrm{DIC}}, \quad p_{\mathrm{DIC}} = 2\ln\mathcal{L}(\boldsymbol{\theta}_p) - 2\langle\ln\mathcal{L}\rangle_P. \quad (1)$$

The first term is given by -2 times the logarithm of the likelihood $\mathcal{L}(\boldsymbol{\theta}) = P(\boldsymbol{d}|\boldsymbol{\theta}, M)$ at some point in parameter space $\boldsymbol{\theta}_p$ and encapsulates how well the model fits the data. Common choices for $\boldsymbol{\theta}_p$ are the mean, maximum of the posterior, or maximum of the likelihood. Here we choose $\boldsymbol{\theta}_p$ to be the maximum of the posterior (MAP). The second term in Eq. (1) is a measure of the model complexity, where the angled brackets denote the average with respect to the posterior $P(\boldsymbol{\theta}|\boldsymbol{d}, M)$. When comparing models, those with a lower DIC are preferred.

The second criterion we employ is the Watanabe-Akaike information criterion (WAIC, also known as widely applicable information criterion, Watanabe & Opper 2010), a Bayesian generalisation of the DIC, as it does not depend on point estimates and has other, desirable properties (Gelman et al. 2014; Vehtari et al. 2017). The WAIC is given by

$$\mathrm{WAIC} = -2\ln\langle\mathcal{L}\rangle_P + 2p_{\mathrm{WAIC}} \quad p_{\mathrm{WAIC}} = 2\ln\langle\mathcal{L}\rangle_P - 2\langle\ln\mathcal{L}\rangle_P. \quad (2)$$

An alternative definition for the model complexities p_{DIC} and p_{WAIC} is based on the variance of the log-likelihood (Watanabe & Opper 2010): $p_{\mathrm{DIC}} = 2p_{\mathrm{WAIC}} = 2\mathrm{Var}_P[\ln\mathcal{L}]$, which corresponds to the Bayesian model dimensionality used in Handley & Lemos (2019). We found this definition to be less stable, however, as in certain cases it predicted model dimensionalities larger than the number of varied parameters. The stability can be improved in the case where the analysis uses many independent data (Gelman et al. 2014; Vehtari et al. 2017) but this does not apply to the present case, where we only have access to $O(1)$ data. For this reason we use the definitions in Eqs. (1) and (2).

The final model selection criterion is the Bayes ratio, the ratio of the evidences of the two models under consideration, where the evidence is defined as

$$Z = \int \mathrm{d}^n\boldsymbol{\theta}\mathcal{L}(\boldsymbol{\theta})\pi(\boldsymbol{\theta}), \quad (3)$$

the integral of the likelihood times the prior $\pi(\boldsymbol{\theta}) = P(\boldsymbol{\theta}|M)$.

To aid interpretability and comparability of these model selection criteria, we put them on a probability scale: each model in the set of models we want to choose from is assigned a weight between 0 and 1, with the weights in the set normalised to 1. These weights can then be interpreted as model probabilities. For the DIC and WAIC, we do so analogously to Akaike weights (Akaike 1978; McElreath 2015; Yao et al. 2018). The weight for each of the N models under consideration is

$$w_i = \frac{\mathrm{e}^{-\frac{1}{2}\Delta_i}}{\sum_{j=1}^{N}\mathrm{e}^{-\frac{1}{2}\Delta_j}}, \quad (4)$$

where Δ_i is the difference in DIC (WAIC) between model i and the model with the lowest DIC (WAIC). The evidences Z_i are already probabilities, such that we only need to normalise them as

$$w_i = \frac{Z_i}{\sum_{j=1}^{N} Z_j}. \quad (5)$$

Unless otherwise specified, the sets of models consist of two members: the fiducial, flat ΛCDM model, and the alternative model under consideration.

Evaluation of the model selection criteria is subject to uncertainties in the sampling and optimisation procedures. We use nested sampling to estimate our posteriors and evidences, where the prior volume of the likelihood contours associated with each sample is not known exactly but only probabilistically (Skilling 2006). We follow Handley & Lemos (2019) and generate many realisations of the prior volumes using ANESTHETIC[5] (Handley 2019) to estimate the uncertainties on our DIC, WAIC, and evidence estimates inherent to the sampling procedure. Other quantities estimated from nested sampling, such as parameter constraints, are in principle also subject to these uncertainties in the prior volumes. We find these uncertainties to be negligible for our parameter constraints, however. For example, in the case of S_8, this sampling uncertainty is of the order of 1% of the parameter uncertainty. We estimate the uncertainty of the value for $\ln\mathcal{L}(\boldsymbol{\theta}_{\mathrm{MAP}})$ from the scatter of 18 optimisation runs with different starting points.

2.4. Tension metrics

There has been a persistent trend of weak lensing analyses finding lower values of S_8 than *Planck*, at varying level of significance (e.g. Heymans et al. 2013; MacCrann et al. 2015; Jee et al. 2016; Joudaki et al. 2017b, 2020; Troxel et al. 2018; Hikage et al. 2019; Hamana et al. 2020; Asgari et al. 2020), with many finding S_8 values that are formally consistent with *Planck*, but none finding values higher than Planck Collaboration VI (2020). Assessing the agreement or disagreement between data sets is thus a key part of this analysis. Here we follow Heymans et al. (2021) in quantifying the concordance or discordance between our results and the temperature and polarisation data from *Planck*.

We consider three tension metrics to quantify the agreement in a single parameter. While all of them agree in the case of Gaussian posterior distributions, their exact values differ when departing from Gaussianity. In case of differences between the metrics, we quote the range spanned by them. The first compares the distance between the means in the parameter θ of two data sets A and B to their variances:

$$T(\theta) = \frac{|\bar{\theta}^{\mathrm{A}} - \bar{\theta}^{\mathrm{B}}|}{\sqrt{\mathrm{Var}[\theta^{\mathrm{A}}] + \mathrm{Var}[\theta^{\mathrm{B}}]}}. \quad (6)$$

This metric is exact in the case of Gaussian posteriors. To address the cases where the posteriors under consideration depart from Gaussianity, we also consider the Hellinger distance

$$d_{\mathrm{H}}^2[p;q] = \frac{1}{2}\int \mathrm{d}\theta\left[\sqrt{p(\theta)} - \sqrt{q(\theta)}\right]^2, \quad (7)$$

where $p(\theta)$ and $q(\theta)$ are the marginal posterior distributions under consideration. Finally, we also check the distribution of

[5] https://github.com/williamjameshandley/anesthetic

the parameter shifts, and its associated tension measure

$$p_S(\boldsymbol{\theta}) = \int_{P(\Delta\boldsymbol{\theta})>P(0)} P(\Delta\boldsymbol{\theta})\mathrm{d}\Delta\boldsymbol{\theta}, \tag{8}$$

where $P(\Delta\boldsymbol{\theta})$ is the distribution of $\Delta\boldsymbol{\theta} = \boldsymbol{\theta}^{\mathrm{A}} - \boldsymbol{\theta}^{\mathrm{B}}$. We refer the reader to Appendix G in Heymans et al. (2021) for details.

Where we want to assess the agreement or disagreement over the whole model, rather than specific parameters, we use the Bayes ratio between a model that jointly describes two data sets and a model that has separate parameters for each of the data sets. The Bayes ratio is, however, dependent on the prior choices. The suspiciousness (Handley & Lemos 2019) approximately cancels this prior dependence by subtracting the Kullback-Leibler divergence between the posterior and prior. As a result, the suspiciousness $\ln S$ can be expressed solely in terms of the expectation values of the log-likelihoods (Heymans et al. 2021):

$$\ln S = \langle \ln \mathcal{L}_{\mathrm{A+B}} \rangle_{P_{\mathrm{A+B}}} - \langle \ln \mathcal{L}_{\mathrm{A}} \rangle_{P_{\mathrm{A}}} - \langle \ln \mathcal{L}_{\mathrm{B}} \rangle_{P_{\mathrm{B}}}. \tag{9}$$

Finally, we also quote the Q_{DMAP} statistics (Raveri & Hu 2019), which measures the change in the best-fit χ^2 values when combining data sets.

3. Models

Here we briefly review the theory behind the ΛCDM extensions investigated in this work, provide arguments that motivate their analysis, and report recent bounds on their parameters.

3.1. Curvature

The most general line element consistent with translational and rotational symmetries (that is, homogeneity and isotropy) reads

$$\mathrm{d}s^2 = -c^2\mathrm{d}t^2 + a^2\left[\mathrm{d}\chi^2 + f_K^2(\chi)\mathrm{d}\Omega^2\right], \tag{10}$$

where c is the speed of light, Ω denotes the solid angle, a is the scale factor at the cosmic time t, χ is the comoving radial coordinate, and

$$f_K(\chi) = \begin{cases} K^{-1/2}\sin\left(K^{1/2}\chi\right) & \text{for } K > 0 \\ \chi & \text{for } K = 0 \\ (-K)^{-1/2}\sinh\left[(-K)^{1/2}\chi\right] & \text{for } K < 0 \end{cases} \tag{11}$$

is the comoving angular diameter distance, with spatial curvature $K = 0$, $K > 0$, and $K < 0$ producing a flat, closed and open geometry, respectively. The background expansion at late times, ignoring radiation terms, then takes the form

$$\left(\frac{H}{H_0}\right)^2 = \Omega_{\mathrm{m}}a^{-3} + (1 - \Omega_{\mathrm{m}} - \Omega_K) + \Omega_K a^{-2}, \tag{12}$$

where $H = \dot{a}/a$, with the spatial curvature parameter defined as $\Omega_K \equiv -(c/H_0)^2K$. The combination of *Planck* and BAO data provides the tightest constraints to date on this parameter, $\Omega_K = -0.0001 \pm 0.0018$ at 68% confidence level (eBOSS Collaboration 2021), while eBOSS BAO data by themselves constrains curvature to $\Omega_K = 0.078^{+0.086}_{-0.099}$. However, *Planck* data alone show at least a 3σ preference for a closed universe, with $\Omega_K = -0.044^{+0.018}_{-0.015}$ (68% CL, but with non-Gaussian tails; Planck Collaboration VI 2020).

The linear power spectrum is computed with CAMB, which uses a form of the primordial power spectrum that allows for both curvature and a tilt ($n_{\mathrm{s}} \neq 1$). While this is a phenomenological model, it is commonly used in cosmological analyses, such as Planck Collaboration VI (2020). Furthermore, we assume that the non-linear growth of structure in a curved universe can be directly inferred from knowledge of the linear power spectrum alone (cf. Mead 2017), which allows us to use the standard HMCODE prescription (Mead et al. 2016).

3.2. Massive neutrinos

The observed neutrino flavour oscillations require at least two of the three neutrino eigenstates $\{m_1, m_2, m_3\}$ to be massive (Pontecorvo 1958; Fukuda et al. 1998; Ahmad et al. 2002), thus cosmologies with $\sum_{i=1}^{3} m_i > 0$ are well-motivated extensions to the base ΛCDM model. Oscillation experiments measure the mass-squared splitting between the mass eigenstates, which provides a lower bound on the sum of neutrino masses. In the normal hierarchy ($m_1 < m_2 < m_3$) $\sum m_\nu \gtrsim 0.06\,\mathrm{eV}$, while in the inverted hierarchy ($m_3 < m_1 < m_2$) $\sum m_\nu \gtrsim 0.1\,\mathrm{eV}$. Direct measurements of the beta decay of tritium have constrained the mass of the anti-electron neutrino to $m_{\nu_{\mathrm{e}}} < 1.1\,\mathrm{eV}$ (Aker et al. 2019) at 90% CL.

Contrary to cold dark matter, cosmological neutrinos possess high thermal velocities which prevents them from clustering on scales smaller than their free-streaming length, thus suppressing the growth of structure (see, e.g. Lesgourgues & Pastor 2006). Therefore the large-scale structure is a sensitive probe of the sum of neutrino masses, with current constraints in the range $\sum m_\nu < 0.14$–$4.5\,\mathrm{eV}$ at 95% CL depending on the particular data set combination and analysis method employed (Lattanzi & Gerbino 2018).

In this work we assume the normal hierarchy, although our data are not sensitive to this choice. The non-linear matter power spectrum is computed with a version of HMCODE (Mead et al. 2016) where we removed the contribution of massive neutrinos from the halo mass in the one-halo term in order to provide a better match of HMCODE to the Mira Titan emulator (Lawrence et al. 2017) for high neutrino masses (cf., Mead et al. 2021). This has a suppressing effect on the highly non-linear portion of the HMCODE prediction that scales with the neutrino fraction, being approximately per-cent level for $\sum m_\nu = 0.06\,\mathrm{eV}$.

3.3. Dark energy equation of state

Although the cosmological constant phenomenology is in remarkable agreement with a diverse array of observations, the physical mechanism driving the late-time cosmic acceleration remains unknown. The simplest possible phenomenological extension to Λ is a smooth evolving dark energy component parametrised by a constant equation of state (e.o.s.) parameter $w < -1/3$, which matches the cosmological constant for $w = -1$. The background expansion in these models is modified as

$$\left(\frac{H}{H_0}\right)^2 = \Omega_{\mathrm{m}}a^{-3} + (1 - \Omega_{\mathrm{m}})\,a^{-3(1+w)}. \tag{13}$$

In principle, Eq. (13) can include the curvature terms of Eq. (12) as well but in this work we only consider the cases of either a non-flat Universe or one with an evolving dark energy component. In our wCDM analysis, we assume a single fluid dark energy model with a constant w and a constant sound-speed of $c_{\mathrm{s}}^2 = 1$ (in natural units).

Previous 3×2pt analyses found $w < -0.73$ at 95% CL, using the previous KiDS release (KiDS-450) combined with

2dFLenS and BOSS spectroscopy (Joudaki et al. 2018), and $w = -0.82^{+0.21}_{-0.20}$ at 68% CL from DES Y1 imaging data alone (Dark Energy Survey Collaboration 2018). This can be compared with constraints from *Planck* temperature and polarisation data, where $w = -1.58^{+0.52}_{-0.41}$ (95% CL; Planck Collaboration VI 2020), and eBOSS BAO data, which constrain $w = -0.69 \pm 0.15$ (68% CL; eBOSS Collaboration 2021). Joint analyses of earlier *Planck* data, together with CMB data from the South Pole Telescope and a range of non-CMB data found $w = -0.989 \pm 0.032$ (68% CL; Park & Ratra 2020). Combining *Planck* temperature and polarisation data, eBOSS BAO data, and the Pantheon SNe sample constrains $w = -1.026 \pm 0.033$ (68% CL; eBOSS Collaboration 2021).

3.4. $f(R)$ gravity

The standard cosmological model rests on the assumption that Einstein's general relativity (GR) is the correct theory of gravity. Departures from GR are tightly constrained on Solar System and astrophysical scales (Will 2014; Abbott et al. 2017; Sakstein 2018; Desmond & Ferreira 2020), but interesting deviations are still possible on larger scales (see, e.g. Joudaki et al. 2018; Dark Energy Survey Collaboration 2019; Spurio Mancini et al. 2019). A breakdown of GR flagged by the large-scale structure statistics would revolutionise the foundations of physics, and could provide an explanation for the observed cosmic acceleration (see, e.g. Koyama 2018; Ferreira 2019).

In this work we focus on $f(R)$ gravity, a popular extension to GR where the Ricci scalar, R, is promoted to a generic non-linear function, $f(R)$. More specifically, we adopt the Hu-Sawicki functional form, where the range of the fifth force – the Compton wavelength – today is given by (Hu & Sawicki 2007)

$$\lambda_{\rm C0} \approx 42 \sqrt{\frac{1}{4-3\Omega_{\rm m}} \frac{|f_{R0}|}{10^{-4}}}\, h^{-1}\,{\rm Mpc}. \tag{14}$$

Here f_{R0} is a parameter controlling the extent of the modification, with GR being recovered for $f_{R0} = 0$. At the level of linear growth the Compton wavelength, $\lambda_{\rm C0}$, acts as a cut-off scale. On scales $\gg\lambda_{\rm C0}$ structures evolve as in GR, whereas on scales $\ll\lambda_{\rm C0}$ the gravitational force is enhanced by 1/3. In the non-linear regime the activation of the chameleon screening (Khoury & Weltman 2004) drives gravity to GR for values $|f_{R0}| \lesssim 10^{-5}$ (see, e.g. Schmidt et al. 2009). Deviations from the ΛCDM background expansion are $O(|f_{R0}|)$ (Hu & Sawicki 2007), and since all the models considered here have $|f_{R0}| \ll 1$ we fix the effective equation of state to $w = -1$. Using a combination of CMB measurements (or priors) and large-scale structure data the most recent analyses find that values as large as $|f_{R0}| \approx 10^{-5}$ are still consistent with observations at 95% CL (e.g. Cataneo et al. 2015; Liu et al. 2016; Alam et al. 2016; Hu et al. 2016).

We compute the non-linear matter power spectrum in $f(R)$ gravity with `ReACT` (Bose et al. 2020), a public C++ library[6] based on the reaction method of Cataneo et al. (2019), which we couple to `HMCODE`. The latter provides the cosmology-dependent reference power spectrum to be corrected by the reaction, therefore properly accounting for modified gravity non-linearities.

[6] https://github.com/nebblu/ReACT

4. Results

We first explore how restricting the KiDS-1000 posterior space, either by fixing a subset of parameters to *Planck* best-fit values (Sect. 4.1) or jointly analysing both KiDS and *Planck* with external data sets (Sect. 4.2), affects the parameter constraints of KiDS-1000 and their agreement with *Planck*. We then explore the effect of extending the parameter space by allowing for curvature (oΛCDM, Sect. 4.3), varying the mass of the neutrinos (νΛCDM, Sect. 4.4), varying the dark energy equation of state (wCDM, Sect. 4.5), or considering $f(R)$-gravity (Sect. 4.6) has on the KiDS-1000 parameter constraints and whether these extended models can solve the observed tension of KiDS-1000 with *Planck*.

Unless noted otherwise, parameter constraints are reported as the mode of the joint posterior (MAP), together with the projected joint highest posterior density (PJ-HPD, for details see Joachimi et al. 2021) credible intervals. The model selection criteria and the S_8 tension metrics for *Planck* are summarised in Tables 2 and 3, respectively. In the case where the numerical values of tension metrics differ, we quote the range spanned by them as a robust estimate of the tension in the presence of non-Gaussian posteriors.

4.1. Fixing the primordial matter power spectrum

The KiDS-1000 cosmic shear and 3×2 pt analyses (Asgari et al. 2021; Heymans et al. 2021) found the amplitude of the measured signal, chiefly dependent on S_8, to be low by about 3σ compared to the value derived from the CMB by *Planck*. The parameter $S_8 = \sigma_8\sqrt{\Omega_{\rm m}/0.3}$ is well suited to summarise weak lensing results but its mapping to the parameters used to parameterise CMB anisotropies is complicated. It is thus not clear whether the observed differences in S_8 are due to differences in the amplitude of the matter power spectrum at early and late times, described by $A_{\rm s}$, or other parameters that affect S_8. To answer this question, we test whether fixing $A_{\rm s}$, the amplitude of the primordial matter power spectrum, to the *Planck* best-fit value ameliorates the observed tension in S_8 when analysing the KiDS-1000 cosmic shear and 3×2 pt data.

The resulting constraints are shown in Fig. 1. We find that fixing $A_{\rm s}$ serves to tighten the cosmic shear constraints along the $\Omega_{\rm m}$–σ_8 degeneracy but does not significantly change the constraints perpendicular to it. This is consistent with the known effect of $A_{\rm s}$ priors primarily affecting the length of the $\Omega_{\rm m}$–σ_8 'banana' (e.g. Joudaki et al. 2017b; Chang et al. 2019; Joachimi et al. 2021) but not constraints on S_8. Fixing $A_{\rm s}$ to the *Planck* best-fit value moves the marginal S_8 posterior for cosmic shear to slightly higher values but also reduces its width, such that the tension remains at 2.8–2.9σ. For the 3×2 pt data, the S_8 constraints remain largely unchanged, with the tension to *Planck* remaining at 2.9–3.0σ. Fixing the tilt of the primordial power spectrum, $n_{\rm s}$, to the *Planck* best-fit value on top of fixing $A_{\rm s}$ does not change these results for either cosmic shear or 3×2 pt. The changes in goodness-of-fit when fixing $A_{\rm s}$ lie within our uncertainties on how well we can estimate the χ^2 at the MAP. The DIC, WAIC, and Bayes ratio do not disfavour a model with fixed $A_{\rm s}$ either (see Table 2 for details).

This highlights that the amplitudes of the two-point statistics of the early-time CMB and the late-time large-scale structure probe different aspects of cosmology. While a model with fixed $A_{\rm s}$ still retains enough freedom to describe the cosmic shear and galaxy clustering data, it reduces the freedom in the other parameters. Notably, while in the fiducial model the

Table 2. Summary of the model selection criteria considered in this work.

Probe	$\Delta\chi^2_{\rm MAP}$	ΔDIC	ΔWAIC	$\Delta \log Z$	$w_{\rm DIC}$	$w_{\rm WAIC}$	$w_{\rm Z}$
Fix $A_{\rm s}$ (Sect. 4.1)							
Cosmic shear	0.05 ± 0.05	-0.84 ± 0.31	-0.54 ± 0.19	0.18 ± 0.12	0.60	0.57	0.55
3×2 pt	0.32 ± 0.36	-0.71 ± 0.71	-0.59 ± 0.48	1.66 ± 0.27	0.59	0.57	0.84
$o\Lambda$CDM (Sect. 4.3)							
Cosmic shear	-1.25 ± 0.08	0.72 ± 0.25	-0.00 ± 0.17	-0.07 ± 0.10	0.41	0.50	0.48
Galaxy clustering	0.23 ± 0.24	3.92 ± 0.55	3.24 ± 0.38	-1.10 ± 0.26	0.13	0.17	0.25
3×2 pt	0.10 ± 0.34	1.24 ± 0.62	0.62 ± 0.38	-1.33 ± 0.24	0.35	0.42	0.21
$\nu\Lambda$CDM (Sect. 4.4)							
Cosmic shear	-1.32 ± 0.06	-0.27 ± 0.25	-0.59 ± 0.16	0.29 ± 0.11	0.53	0.57	0.57
Galaxy clustering	-0.03 ± 0.29	2.38 ± 0.52	1.77 ± 0.34	0.23 ± 0.26	0.24	0.29	0.56
3×2 pt	-0.96 ± 0.47	1.59 ± 0.70	0.38 ± 0.39	0.40 ± 0.22	0.31	0.45	0.60
wCDM (Sect. 4.5)							
Cosmic shear	-1.58 ± 0.13	2.43 ± 0.26	0.92 ± 0.16	-0.38 ± 0.11	0.23	0.39	0.41
Galaxy clustering	-0.20 ± 0.31	4.75 ± 0.59	3.24 ± 0.37	-0.75 ± 0.29	0.09	0.17	0.32
3×2 pt	0.34 ± 0.37	1.53 ± 0.61	1.28 ± 0.40	-1.85 ± 0.25	0.32	0.35	0.14
$f(R)\Lambda$CDM (Sect. 4.6)							
Cosmic shear	-0.56 ± 0.07	0.58 ± 0.28	0.09 ± 0.18	-0.21 ± 0.13	0.43	0.49	0.45
Baryon model (Appendix A)							
Cosmic shear	0.32 ± 0.07	-0.54 ± 0.31	-0.05 ± 0.19	0.21 ± 0.14	0.57	0.51	0.55
3×2 pt	0.52 ± 0.32	-1.50 ± 0.69	-1.01 ± 0.46	0.20 ± 0.27	0.68	0.62	0.55

Notes. The first column lists the probes and models under consideration in this work. The second column list the change in the χ^2 value at the maximum of the posterior compared to the fiducial results of Asgari et al. (2021) and Heymans et al. (2021). The quoted uncertainty is the scatter between optimisation runs. Columns 3–5 list the three model selection criteria considered in this work: DIC (Eq. (1)), WAIC (Eq. (2)), and change in the evidence (Eq. (3)), with the uncertainties due to the stochasticity of nested sampling estimates. The last three columns list the model probabilities based on the three selection criteria with respect to the fiducial, flat ΛCDM model, as defined in Sect. 2.3. The relative uncertainty on the model probabilities are of the order of 10–20% but for clarity we do not quote them here.

Hubble parameter h is largely uncorrelated with $\Omega_{\rm m}$ and σ_8, fixing $A_{\rm s}$ induces strong correlations of these parameters with h, as seen on the bottom row of Fig. 1 (cf., Sánchez 2020). Breaking the induced $\Omega_{\rm m}$–h degeneracy by adding independent information on $\Omega_{\rm m}$ that is consistent with *Planck*, for example through the BAO in the 3×2 pt data, results in pulling the inferred h constraints down to the *Planck* values. On the other hand, breaking the σ_8–h degeneracy by restricting σ_8 to *Planck* values results in higher h values, inconsistent with *Planck*. In the parameter S_8, the $\Omega_{\rm m}$–h and σ_8–h degeneracies cancel out, so that the S_8 constraints and tension with *Planck* are largely independent of h.

4.2. External data: SNe and CMB lensing

Current weak lensing surveys cannot by themselves constrain both σ_8 and $\Omega_{\rm m}$; the two parameters are degenerate with each other, with the width of degeneracy given by the uncertainty on $\sim S_8$, and its length largely set by the priors (Joudaki et al. 2017b; Joachimi et al. 2021). Including external data allows us to break this degeneracy. In our 3×2 pt analysis, this is achieved by the inclusion of spectroscopic galaxy clustering data, which primarily provides constraints on $\Omega_{\rm m}$ through the BAO feature.

Here we explore two different data sets that allow the breaking of the σ_8–$\Omega_{\rm m}$ degeneracy; supernovae and lensing of the CMB. Supernovae provide an independent, low-redshift estimate of $\Omega_{\rm m}$, with our prior on $\omega_{\rm c}$ (see Table 1) being informed by the 5σ constraints on $\Omega_{\rm m}$ derived in Scolnic et al. (2018). In CMB lensing, light from the CMB is lensed by the intervening structure between $z = 0$ and the surface of last scattering, as detected in the CMB temperature and polarisation anisotropies (Lewis & Challinor 2006). CMB lensing is highly complementary to galaxy lensing, as it exhibits a different degeneracy in the σ_8–$\Omega_{\rm m}$ plane (Planck Collaboration VIII 2020).

We jointly analyse our cosmic shear bandpower data vector with the Pantheon (Scolnic et al. 2018) likelihood, marginalising over the absolute calibration parameter M. The resulting parameter constraints are summarised in Fig. 2. The addition of Pantheon data constrains the matter density to $\Omega_{\rm m} = 0.297^{+0.021}_{-0.018}$ and the amount of matter clustering to $\sigma_8 = 0.769^{+0.028}_{-0.041}$. This tightens the constraints on S_8 by ∼45% to $S_8 = 0.765^{+0.015}_{-0.022}$. The increase in constraining power is largely driven by the tight constraints on $\Omega_{\rm m}$ and the residual correlation between $\Omega_{\rm m}$ and S_8 in our bandpower cosmic shear results. This is made evident by considering the constraints on the parameter $\Sigma_8 = \sigma_8\,(\Omega_{\rm m}/0.3)^{0.58}$, which provides a better description of the degeneracy direction in $\Omega_{\rm m}$ and σ_8 (Asgari et al. 2021): the constraints on Σ_8 tighten by only ∼5% when jointly analysing cosmic shear with Pantheon data.

The results of the joint analysis of our 3×2 pt data with Pantheon do not differ from the fiducial 3×2 pt analysis. The galaxy clustering data already provides stringent constraints on $\Omega_{\rm m}$, such that the addition of the fully consistent, but weaker, constraints on $\Omega_{\rm m}$ from Pantheon does not further improve the constraining power in flat ΛCDM. Similarly, adding the Pantheon likelihood to the *Planck* TTTEEE+lowE likelihood does not appreciably change the *Planck* constraints. The tension in S_8 thus remains at 3.0σ when analysing both KiDS-1000 and *Planck* jointly with SNe data. Since the two estimates of S_8 are not independent anymore, the tension is to be understood as conditioned on the SNe data. Using a prior on h from Riess et al. (2019) based on the local distance ladder does not change the KiDS-1000 cosmic shear or 3×2 pt results.

Table 3. Summary of the tension metrics considered in this work.

Probe	$T(S_8)$	$H(S_8)$	$p_S(S_8)$
Fiducial (flat ΛCDM)			
Cosmic shear	2.8σ	3.1σ	3.2σ
Galaxy clustering	2.1σ	2.1σ	2.1σ
3×2 pt	3.1σ	3.1σ	3.1σ
Fix A_s (Sect. 4.1)			
Cosmic shear	2.9σ	2.8σ	2.9σ
3×2 pt	2.9σ	2.9σ	3.0σ
SNe (Sect. 4.2)			
Cosmic shear	3.0σ	3.0σ	3.0σ
3×2 pt	3.1σ	3.1σ	3.0σ
CMB lensing (Sect. 4.2)			
Cosmic shear	3.0σ	3.1σ	3.0σ
3×2 pt	2.8σ	2.8σ	2.8σ
$o\Lambda$CDM (Sect. 4.3)			
Cosmic shear	2.4σ	2.5σ	2.6σ
Galaxy clustering	2.4σ	2.4σ	2.6σ
3×2 pt	3.3σ	2.9σ	3.0σ
$\nu\Lambda$CDM (Sect. 4.4)			
Cosmic shear	2.8σ	2.9σ	2.9σ
Galaxy clustering	1.8σ	1.8σ	1.8σ
3×2 pt	3.4σ	3.4σ	3.3σ
wCDM (Sect. 4.5)			
Cosmic shear	1.3σ	1.3σ	1.3σ
Galaxy clustering	2.1σ	2.1σ	2.1σ
3×2 pt	1.8σ	1.8σ	1.7σ
Baryon model (Appendix A)			
Cosmic shear	2.3σ	2.4σ	2.5σ
3×2 pt	2.9σ	2.9σ	2.9σ

Notes. The first column lists the probes and models under consideration in this work. The last three columns list the tension in S_8 with *Planck* TTTEEE+lowE data using the tension metric $T(\theta)$ (Eq. (6)), the Hellinger distance (Eq. (7)), and the parameter shift distribution (Eq. (8)).

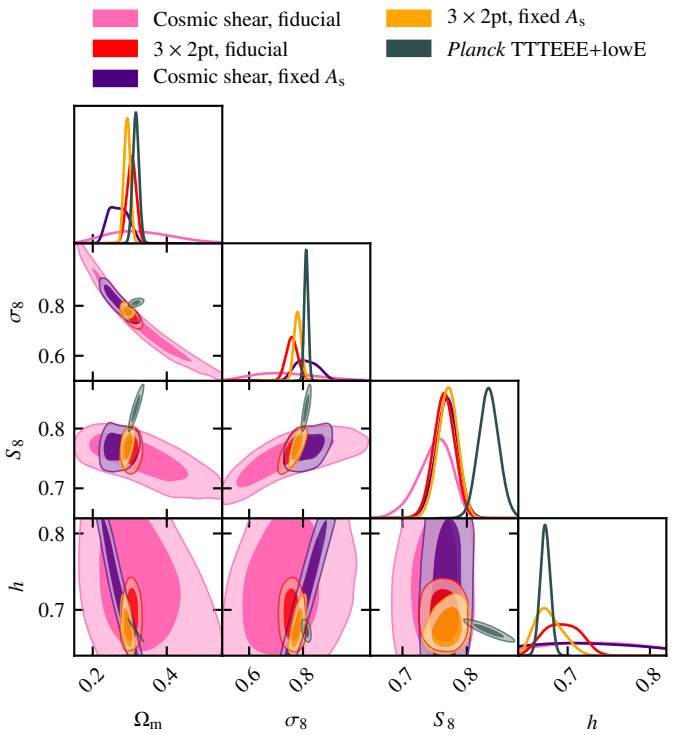

Fig. 1. KiDS-1000 cosmic shear and 3×2 pt parameter constraints when keeping the amplitude of the primordial power spectrum A_s fixed to the *Planck* best-fit value. The pink (cosmic shear) and red (3×2 pt) contours are the fiducial setup, while the purple (cosmic shear) and orange (cosmic shear) contours show the constraints when A_s is being kept fixed. The grey contours denote the *Planck* TTTEEE+lowE results.

Planck Collaboration VIII (2020) analysed the reconstructed lensing potential, as inferred from the CMB temperature and polarisation data, which constrains the parameter combination $\sim\sigma_8\Omega_m^{0.25}$. This parameter combination is more sensitive to σ_8 than is the case for S_8 and when combined with the galaxy lensing, breaks both degeneracies. When jointly analysing our cosmic shear, respectively 3×2 pt, data with the CMB lensing data[7], we do so with the KiDS-1000 prior choices (Joachimi et al. 2021; Heymans et al. 2021). They chiefly differ from those adopted in Planck Collaboration VIII (2020) in h and n_s: the KiDS-1000 prior on h is uniform on the range $[0.64, 0.82]$, approximately encompassing the 5σ ranges of both the CMB constraints from Planck Collaboration VI (2020) and the local distance ladder of Riess et al. (2019), while the CMB lensing analysis of Planck Collaboration VIII (2020) adopted a very wide prior[8] of $[0.4, 1.0]$. Conversely, the KiDS-1000 prior on n_s is uniform on $[0.84, 1.1]$, while Planck Collaboration VIII (2020) imposes a tight Gaussian prior of $n_s \sim \mathcal{N}(0.96, 0.02)$. These different prior choices do not affect the posteriors in the region of parameter space where the galaxy and CMB lensing constraints overlap, but they affect the range of Ω_m values allowed by CMB lensing.

Figure 3 illustrates the joint constraints of KiDS-1000 cosmic shear and CMB lensing, as well as KiDS-1000 3×2 pt and CMB lensing. The combination of KiDS-1000 cosmic shear and CMB lensing constrains the matter density to $\Omega_m = 0.269^{+0.026}_{-0.029}$, and the clustering amplitude to $\sigma_8 = 0.81^{+0.047}_{-0.029}$, with $S_8 = 0.768^{+0.017}_{-0.013}$. The addition of CMB lensing also improves the 3×2 pt constraints; we find $\Omega_m = 0.307^{+0.008}_{-0.013}$, $\sigma_8 = 0.769^{+0.022}_{-0.010}$, and $S_8 = 0.779^{+0.013}_{-0.013}$. The addition of CMB lensing data thus causes a ∼75% and ∼35% improvement in the constraining power on S_8 for cosmic shear and 3×2 pt, respectively. As in the case of the joint-analysis with SNe data, the improvement on the cosmic shear S_8 constraints is driven by the residual correlation between Ω_m and S_8, with the constraints on Σ_8 tightening by only ∼5%.

Both the cosmic shear and 3×2 pt-inferred marginal distributions for S_8 are narrowed and move to somewhat higher values. For cosmic shear, the tension conditioned on the CMB lensing data remains at 3.0–3.1σ, while for 3×2 pt it is slightly reduced to 2.8σ (cf., Table 3).

4.3. Curvature

We vary Ω_K uniformly in the interval $[-0.4, 0.4]$, the results of which are shown in Fig. 4. Our cosmic shear data do not meaningfully constrain Ω_K but galaxy clustering by itself gives $\Omega_K = -0.07^{+0.12}_{-0.09}$, which is improved on by the full 3×2 pt data vector to

$$\Omega_K = 0.011^{+0.054}_{-0.057}.$$

[7] For technical reasons, we use the COBAYA (Torrado & Lewis 2020) CMB lensing likelihood https://github.com/CobayaSampler/planck_lensing_external

[8] Sampling in Planck Collaboration VIII (2020) was performed with a uniform prior on θ_{MC}, but restricted to the range $H_0 \in [0.4, 1.0]$.

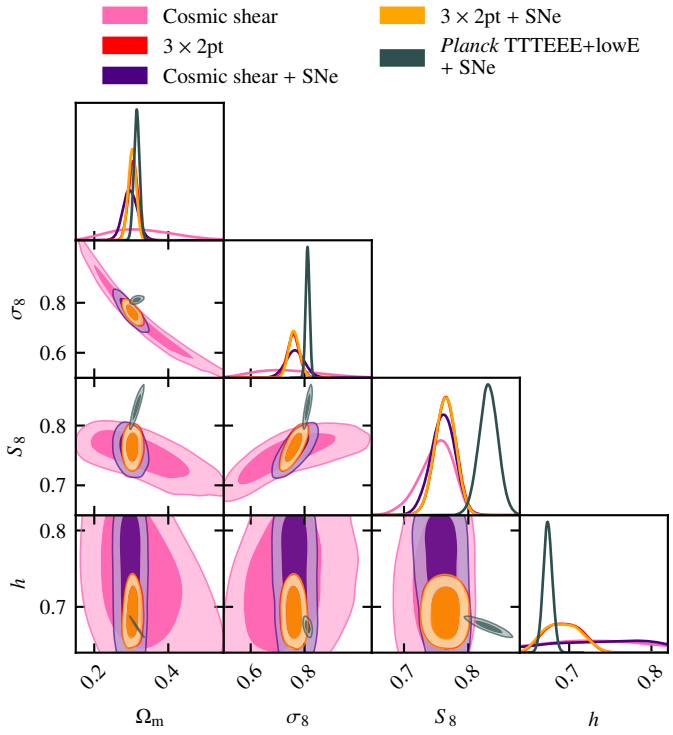

Fig. 2. Joint constraints of KiDS-1000 cosmic shear and 3 × 2 pt data with the Pantheon supernova data set (Scolnic et al. 2018). The fiducial cosmic shear bandpower and 3 × 2 pt results are shown in pink and red, respectively. The joint constraints with Pantheon are denoted in purple and orange, respectively. For 3×2 pt, the addition of SNe data leaves the constraints virtually unchanged, such that the orange and red contours overlap. Finally, the corresponding *Planck* TTTEEE+lowE + Pantheon constraints are in grey.

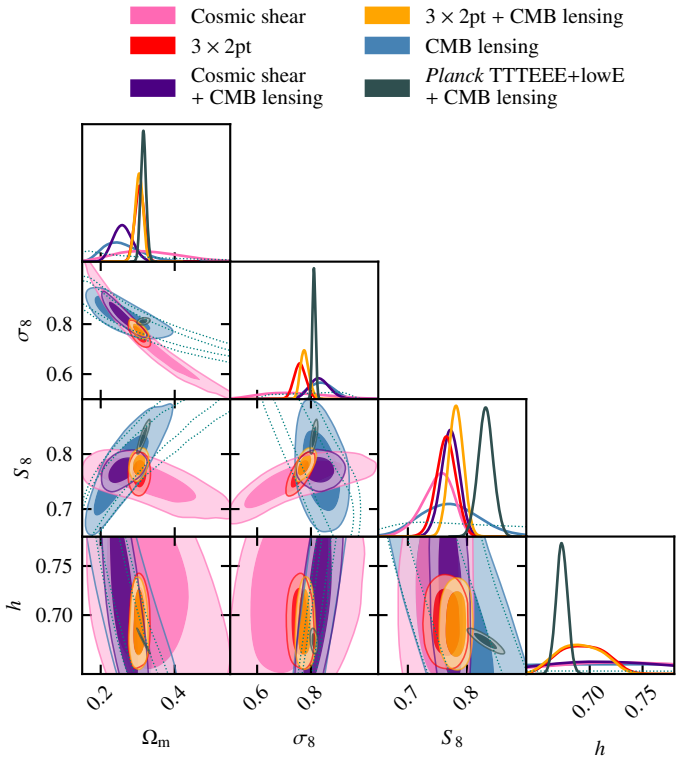

Fig. 3. Joint constraints of KiDS-1000 cosmic shear and 3 × 2 pt data with CMB lensing data from Planck Collaboration VIII (2020). The fiducial cosmic shear bandpower and 3 × 2 pt results are shown in pink and red, respectively, while the joint constraints with CMB lensing are shown in purple and orange, respectively. The *Planck* CMB lensing constraints, with the priors matched to the KiDS analysis, are denoted in solid blue, whereas the fiducial CMB lensing results from Planck Collaboration VIII (2020) are denoted with a dotted line. The *Planck* TTTEEE+lowE + CMB lensing constraints are shown in grey.

The *Planck* CMB constraints on $o\Lambda$CDM have significant posterior mass at low values of h, outside the KiDS prior range. For a comparison to our results, we analyse the *Planck* temperature and polarisation data with the KiDS priors, where we find a disagreement at 2.9−3.3σ in S_8. The $o\Lambda$CDM constraints as reported by Planck Collaboration VI (2020) prefer a much higher value of S_8 due to the preference for high Ω_m. Compared to these results, the tension is >4σ. While the priors differ in this case, this has little effect, since our 3 × 2 pt results would not change significantly if the h prior were relaxed, as the S_8 and h are largely uncorrelated for 3 × 2 pt and there is little likelihood mass outside the h prior. Our setup of harmonising the priors thus provides a lower bound on the tension in S_8.

The model selection criteria show no preference for the $o\Lambda$CDM model, with it being slightly disfavoured for galaxy clustering and 3 × 2 pt but not at any level of meaningful significance.

4.4. Massive neutrinos

The results of varying the sum of the neutrino masses $\sum m_\nu$ uniformly between 0 and 3 eV are shown in Fig. 5. We find that our 3 × 2 pt data provide marginal constraints on the sum of neutrino masses of

$$\sum m_\nu < 1.76\,\mathrm{eV} \quad (95\%\,\mathrm{CL}).$$

Allowing the neutrino mass to vary does not affect the cosmic shear constraints but loosens the 3 × 2 pt constraints along the cosmic shear σ_8−Ω_m degeneracy. This serves to increase the tension with *Planck* in S_8 to 3.3−3.4σ.

Our constraints on $\sum m_\nu$ improve upon earlier results based on KiDS-450, 2dFLenS and BOSS RSD of Joudaki et al. (2018), who found $\sum m_\nu < 2.2$ eV. They also compare favourably to constraints from DES Y1 3 × 2 pt data, when $\sum m_\nu$ was allowed to vary over a larger range[9], which yielded $\sum m_\nu < 2.3$ eV. They are, however, significantly weaker than other cosmological constraints reported in the literature that include CMB data. We believe that combining our constraints with *Planck* in light of the persistent S_8 tension would not be a consistent approach, however. The joint analysis of *Planck* and DES Y1 data yielded weaker upper limits than just *Planck* data by themselves due to a slight preference of the DES Y1 data for lower clustering amplitudes than *Planck* (Dark Energy Survey Collaboration 2018; Planck Collaboration VI 2020). As our 3 × 2 pt data similarly prefer low clustering amplitudes and do no exclude high neutrino masses, we do not expect a joint analysis with *Planck* to improve upon *Planck*-only constraints on $\sum m_\nu$.

The model selection criteria indicate no preference of a $\nu\Lambda$CDM model over a model where the neutrino mass is fixed to 0.06 eV.

[9] The constraint is derived from the reanalysis of DES Y1 data in Planck Collaboration VI (2020), available on the *Planck* Legacy Archive (`https://pla.esac.esa.int`).

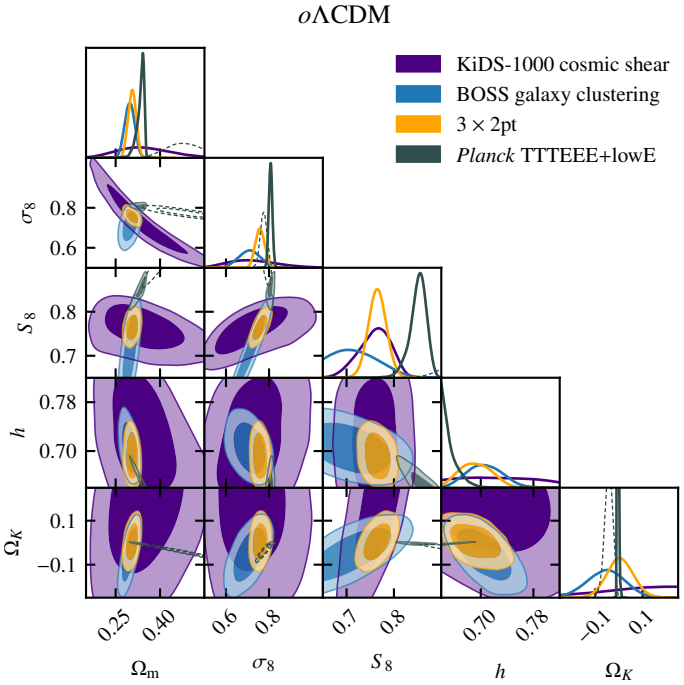

Fig. 4. Parameter constraints for a $o\Lambda$CDM model for KiDS-1000 cosmic shear (purple), BOSS DR12 galaxy clustering (blue), and 3×2 pt (orange). The *Planck* constraints with priors matched to the KiDS setup are shown in solid grey, whereas the fiducial results from Planck Collaboration VI (2020) are indicated with a dotted line.

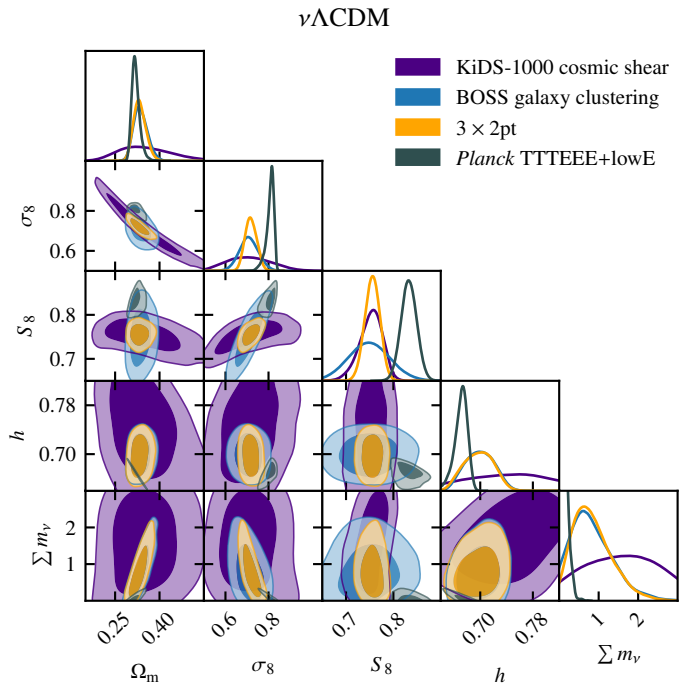

Fig. 5. Parameter constraints for a $\nu\Lambda$CDM model for KiDS-1000 cosmic shear (purple) and 3×2 pt (orange). The *Planck* TTTEEE+lowE constraints are shown in solid grey.

4.5. Dark energy equation of state

We vary the dark energy equation of state parameter w with a uniform prior of $w \sim \mathcal{U}(-3.0, -0.33)$. The upper end of the prior range is chosen such that the cosmic expansion is accelerating. To allow comparison with the flat ΛCDM results, we again keep

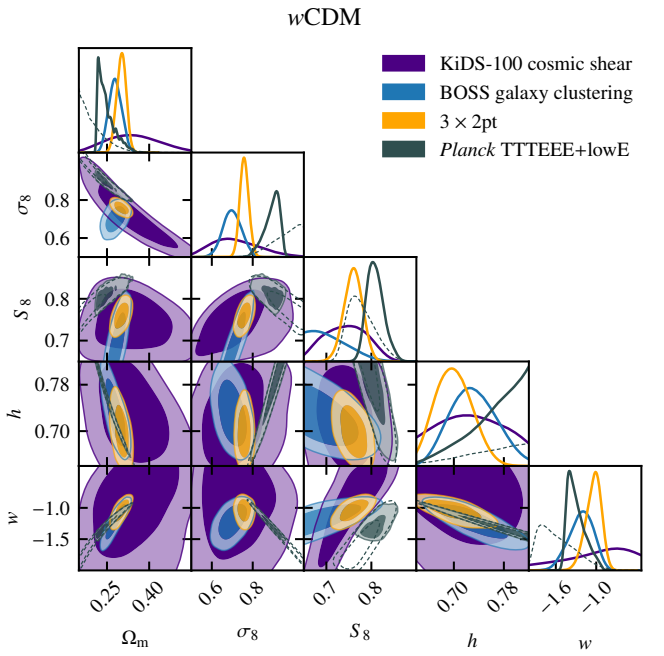

Fig. 6. Parameter constraints for a wCDM model for KiDS-1000 cosmic shear (purple), BOSS DR12 galaxy clustering (blue), and 3×2 pt (orange). The *Planck* constraints with priors matched to the KiDS setup are shown in solid grey, while the fiducial results from Planck Collaboration VI (2020) are indicated with a dotted line.

the priors on the other parameters the same. The prior excludes parts of the *Planck* wCDM posterior space with high values of $h > 0.82$. This region is, however, inconsistent with local measurements (Dhawan et al. 2020) and the combined constraints from *Planck* and SNe or BAO (eBOSS Collaboration 2021).

We present our wCDM constraints in Fig. 6. While our cosmic shear data by themselves do not provide meaningful constraints on w, the clustering of the BOSS galaxies does, for which we find $w = -1.05^{+0.21}_{-0.26}$. The combination of cosmic shear and galaxy clustering improves the parameter constraints by a factor of about two, with our 3×2 pt constraints being

$$w = -0.99^{+0.11}_{-0.13}.$$

Among the extensions to the flat ΛCDM model considered in this work, a wCDM model reduces the observed tension on S_8 the most, to 1.3σ and $1.7-1.8\sigma$, respectively for cosmic shear and 3×2 pt. The tension in S_8 has disappeared due to the marginal *Planck* constraints on this parameter weakening and preferring lower values, especially when allowing for a wide prior in h, mirroring previous findings in weak lensing and 3×2 pt analyses (Joudaki et al. 2017a, 2018). We test whether this newfound agreement in S_8 extends to other parameters. Specifically we assess the agreement in the S_8–w parameter space, as well as the agreement on the whole shared parameter space, following the approach in Heymans et al. (2021).

To quantify the agreement in the two-dimensional S_8–w parameter space, we use the parameter shift statistic Eq. (8). In this space, the tension between our 3×2 pt constraints and *Planck* is 3.2σ. Over the full, six-dimensional shared parameter space, there is a 2.1σ tension according the suspiciousness statistic (Handley & Lemos 2019) and a 2.4σ tension according to the $Q_{\rm DMAP}$ statistic (Raveri & Hu 2019). The Bayes ratio by contrast is 9 ± 3, corresponding to model probabilities of 0.89 vs 0.11 in favour of a single cosmology for both *Planck* and our

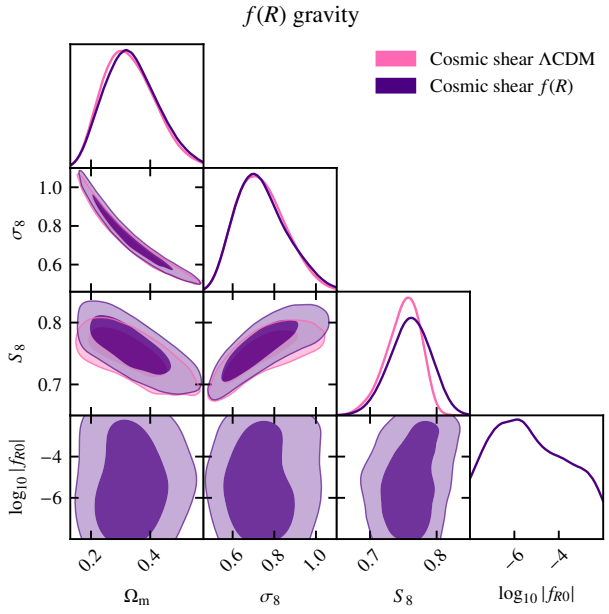

Fig. 7. Parameter constraints for a $f(R)$-gravity model for KiDS-1000 cosmic shear (purple), compared to a flat ΛCDM model (pink).

low-redshift data. The Bayes ratio is generally biased towards concordance however, due to essentially double-counting the prior volumes in the case of separate models. Our model selection criteria do not favour a wCDM model but they also do not exclude it at any level of meaningful significance.

4.6. Modified gravity

We model the full non-linear effect of $f(R)$ gravity on the matter power spectrum using the reaction formalism (Cataneo et al. 2019). The implementation in REACT (Bose et al. 2020) is currently restricted to modelling the matter power spectrum and does not support modelling of non-linear galaxy bias in modified gravity yet. We therefore only consider cosmic shear data here.

We sample $\log_{10}|f_{R0}|$ from a uniform prior $\log_{10}|f_{R0}| \sim \mathcal{U}(-8,-2)$ but find that our current cosmic shear data cannot constrain this parameter within this range, as shown in Fig. 7. While previous work, such as Harnois-Déraps et al. (2015), reported constraints of $\log_{10}|f_{R0}| < -4$ from cosmic shear alone, they did not marginalise over cosmological or nuisance parameters. Future stage IV weak lensing surveys will be able to provide tight constraints on modified gravity models, however, such as $f(R)$ gravity and the DGP (Dvali et al. 2000) braneworld models (Bose et al. 2020).

Allowing f_{R0} to vary extends the allowed values of S_8 to slightly higher values and could thus in principle serve to reduce the tension with *Planck*. This is due to the modified gravity linear power spectrum being enhanced in the presence of $f(R)$ gravity, and the derived values of σ_8 are therefore higher (Planck Collaboration XIV 2016; Wang 2020). The same effect moves the *Planck* contours to higher S_8 as well, however, such that this is an unlikely mechanism to resolve the observed S_8 tension.

5. Conclusions

We analysed the KiDS-1000 cosmic shear data and its combination with BOSS and 2dFLenS into a 3×2 pt data vector in light of extensions to the flat ΛCDM concordance model of cosmology, external data sets, and restricting the freedom of the model.

We found that restricting the freedom of the model to set the amplitude of the primordial power spectrum through A_s does not, maybe surprisingly, resolve the tension with *Planck* in the late-time amplitude parameter S_8.

Jointly analysing our cosmic shear and 3 × 2 pt data with external data sets, namely Type Ia SNe and CMB lensing, serves to break parameter degeneracies, improving the KiDS-1000 cosmic shear constraints in S_8 by ∼45% in case of SNe, and ∼75% in the case of CMB lensing. The improvement on the cosmic shear constraints is more modest at ∼5% when considering the parameter $\Sigma_8 = \sigma_8(\Omega_m/0.3)^{0.58}$, which captures the Ω_m–σ_8 degeneracy better. Neither of these external data sets are able to pull the *Planck* and KiDS-1000 constraints on S_8 closer together, however.

Using three model selection criteria, we assessed whether the data prefer a model other than flat ΛCDM but we found that none of the extensions considered are favoured or disfavoured. We provide constraints independent of the CMB on the curvature $\Omega_K = 0.011^{+0.054}_{-0.057}$ and dark energy equation of state parameter $w = -0.99^{+0.11}_{-0.13}$, both of which are fully consistent with their flat ΛCDM values. The constraints on w are tighter than those from either eBOSS BAO or *Planck* temperature and polarisation data alone but weaker than their combination. Neither of these extensions are preferred by the data over the fiducial flat ΛCDM model according to a range of model selection criteria.

Our data are only able to provide weak constraints on the sum of the neutrino masses $\sum m_\nu < 1.76\,\mathrm{eV}$ at 95% CL. They are, however, independent of CMB data. We use a full non-linear modelling for the matter power spectrum to constrain $f(R)$ gravity but find that current weak lensing data can not constrain f_{R0} by itself. Future weak lensing data, as well as the joint analysis with external data sets will be able to improve these constraints significantly (Bose et al. 2020).

We find that the ∼3σ tension with *Planck* CMB data that was found in Asgari et al. (2021) and Heymans et al. (2021) is not resolved by either extending the parameter space beyond flat ΛCDM, or by restricting it through fixing the amplitude of the primordial power spectrum to the *Planck* best-fit value. To further our understanding of this difference between the early and late-time Universe, we look forward with anticipation to the upcoming independent weak lensing analyses from the Dark Energy Survey and Hyper Suprime-Cam Survey.

Acknowledgements. We thank Antony Lewis for prompting the investigation of the effect of fixing A_s and Will Handley for useful discussions. The figures in this work were created with MATPLOTLIB (Hunter 2007) and GETDIST, making use of the NUMPY (Oliphant 2006) and SCIPY (Jones et al. 2001) software packages. This project has received significant funding from the European Union's Horizon 2020 research and innovation programme. We thank and acknowledge support from: the European Research Council under grant agreement No. 647112 (TT, MA, MCa, CH, CL, and BG), No. 770935 (HHi, AHW, and AD) and No. 693024 (SJ) in addition to the Marie Skłodowska-Curie grant agreements No. 797794 (TT) and No. 702971 (AM). We also acknowledge support from the Max Planck Society and the Alexander von Humboldt Foundation in the framework of the Max Planck-Humboldt Research Award endowed by the Federal Ministry of Education and Research (CH, FK); the Swiss National Science Foundation Professorship grant No. 170547 (BB and LL); the Deutsche Forschungsgemeinschaft Heisenberg grant Hi 1495/5-1 (HHi); the Netherlands Organisation for Scientific Research Vici grant 639.043.512 (HHo, AK); the Alexander von Humboldt Foundation (KK); the Polish Ministry of Science and Higher Education through grant DIR/WK/2018/12, and the Polish National Science Center through grants no. 2018/30/E/ST9/00698 and 2018/31/G/ST9/03388 (MB); the Royal Society through an Enhancement Award RGF/EA/181006 (BG); the Australian Research Council grants DP160102235 and CE17010013 (KG); the Beecroft Trust (SJ); the NSFC of China under grant 11973070, the Shanghai Committee of Science and Technology grant No.19ZR1466600, and the Key Research Program

of Frontier Sciences, CAS, Grant No. ZDBS-LY-7013 (HYS). Funding for SDSS-III has been provided by the Alfred P. Sloan Foundation, the Participating Institutions, the National Science Foundation, and the US Department of Energy Office of Science. The SDSS-III website is http://www.sdss3.org/. SDSS-III is managed by the Astrophysical Research Consortium for the Participating Institutions of the SDSS-III Collaboration including the University of Arizona, the Brazilian Participation Group, Brookhaven National Laboratory, Carnegie Mellon University, University of Florida, the French Participation Group, the German Participation Group, Harvard University, the Instituto de Astrofisica de Canarias, the Michigan State/Notre Dame/JINA Participation Group, Johns Hopkins University, Lawrence Berkeley National Laboratory, Max Planck Institute for Astrophysics, Max Planck Institute for Extraterrestrial Physics, New Mexico State University, New York University, Ohio State University, Pennsylvania State University, University of Portsmouth, Princeton University, the Spanish Participation Group, University of Tokyo, University of Utah, Vanderbilt University, University of Virginia, University of Washington, and Yale University. Based on data products from observations made with ESO Telescopes at the La Silla Paranal Observatory under programme IDs 177.A-3016, 177.A-3017, and 177.A-3018. Author contributions: All authors contributed to the development and writing of this paper. The authorship list is given in three groups: the lead author (TT) followed by two alphabetical groups. The first alphabetical group includes those who are key contributors to both the scientific analysis and the data products. The second group covers those who have either made a significant contribution to the data products, or to the scientific analysis.

References

Abbott, B., Abbott, R., Abbott, T. D., et al. 2017, ApJ, 848, L13
Ahmad, Q. R., Allen, R. C., Andersen, T. C., et al. 2002, Phys. Rev. Lett., 89, 011301
Akaike, H. 1978, J. R. Stat. Soc. Ser. D (Stat.), 27, 217
Aker, M., Altenmüller, K., Arenz, M., et al. 2019, Phys. Rev. Lett., 123, 221802
Alam, S., Ho, S., & Silvestri, A. 2016, MNRAS, 456, 3743
Alam, S., Ata, M., Bailey, S., et al. 2017, MNRAS, 470, 2617
Amon, A., Heymans, C., Klaes, D., et al. 2018, MNRAS, 477, 4285
Asgari, M., Tröster, T., Heymans, C., et al. 2020, A&A, 634, A127
Asgari, M., Lin, C.-A., Joachimi, B., et al. 2021, A&A, 645, A104
Beutler, F., Seo, H.-J., Saito, S., et al. 2017, MNRAS, 466, 2242
Blake, C., Amon, A., Childress, M., et al. 2016, MNRAS, 462, 4240
Blake, C., Amon, A., Asgari, M., et al. 2020, A&A, 642, A158
Bose, B., Cataneo, M., Tröster, T., et al. 2020, MNRAS, 498, 4650
Cataneo, M., Rapetti, D., Schmidt, F., et al. 2015, Phys. Rev., D, 92, 044009
Cataneo, M., Lombriser, L., Heymans, C., et al. 2019, MNRAS, 488, 2121
Chang, C., Wang, M., Dodelson, S., et al. 2019, MNRAS, 482, 3696
d'Amico, G., Gleyzes, J., Kokron, N., et al. 2020, JCAP, 2020, 005
Dark Energy Survey Collaboration (Abbott, T. M. C., et al.) 2018, Phys. Rev. D, 98, 043526
Dark Energy Survey Collaboration (Abbott, T. M. C., et al.) 2019, Phys. Rev. D, 99, 123505
Dawson, K. S., Schlegel, D. J., Ahn, C. P., et al. 2013, AJ, 145, 10
Desmond, H., & Ferreira, P. G. 2020, Phys. Rev., D, 102, 104060
Dhawan, S., Brout, D., Scolnic, D., et al. 2020, ApJ, 894, 54
Di Valentino, E., Melchiorri, A., & Silk, J. 2020, Nat. Astron., 4, 196
Dvali, G., Gabadadze, G., & Porrati, M. 2000, Phys. Lett. B, 485, 208
eBOSS Collaboration (Alam, S., et al.) 2021, Phys. Rev. D, 103, 083533
Efstathiou, G., & Gratton, S. 2020, MNRAS, 496, L91
Feroz, F., & Hobson, M. P. 2008, MNRAS, 384, 449
Feroz, F., Hobson, M. P., & Bridges, M. 2009, MNRAS, 398, 1601
Feroz, F., Hobson, M. P., Cameron, E., & Pettitt, A. N. 2019, Open J. Astrophys., 2, 10
Ferreira, P. G. 2019, ARA&A, 57, 335
Freedman, W. L., Madore, B. F., Hoyt, T., et al. 2020, ApJ, 891, 57
Fukuda, Y., Hayakawa, T., Ichihara, E., et al. 1998, Phys. Rev. Lett., 81, 1562
Gelman, A., Hwang, J., & Vehtari, A. 2014, Stat. Comput., 24, 997
Giblin, B., Heymans, C., Asgari, M., et al. 2021, A&A, 645, A105
Hamana, T., Shirasaki, M., Miyazaki, S., et al. 2020, PASJ, 72, 16
Handley, W. 2019, J. Open Sour. Softw., 4, 1414
Handley, W. 2021, Phys. Rev., D, 103, 041301
Handley, W., & Lemos, P. 2019, Phys. Rev., D, 100, 043504
Harnois-Déraps, J., Munshi, D., Valageas, P., et al. 2015, MNRAS, 454, 2722
Hartlap, J., Simon, P., & Schneider, P. 2007, A&A, 464, 399
Heymans, C., Grocutt, E., Heavens, A., et al. 2013, MNRAS, 432, 2433
Heymans, C., Tröster, T., Asgari, M., et al. 2021, A&A, 646, A140
Hikage, C., Oguri, M., Hamana, T., et al. 2019, PASJ, 71, 43
Hildebrandt, H., van den Busch, J. L., Wright, A. H., et al. 2021, A&A, 647, A124
Hu, W., & Sawicki, I. 2007, Phys. Rev., D, 76, 064004
Hu, B., Raveri, M., Rizzato, M., & Silvestri, A. 2016, MNRAS, 459, 3880
Hunter, J. D. 2007, Comput. Sci. Eng., 9, 90
Ivanov, M. M., Simonović, M., & Zaldarriaga, M. 2020, JCAP, 2020, 042
Jee, M. J., Tyson, J. A., Hilbert, S., et al. 2016, ApJ, 824, 77
Joachimi, B., Lin, C. A., Asgari, M., et al. 2021, A&A, 646, A129
Johnson, A., Blake, C., Amon, A., et al. 2017, MNRAS, 465, 4118
Jones, E., Oliphant, T., Peterson, P., et al. 2001, SciPy: Open Source Scientific Tools for Python
Joudaki, S., Mead, A., Blake, C., et al. 2017a, MNRAS, 471, 1259
Joudaki, S., Blake, C., Heymans, C., et al. 2017b, MNRAS, 465, 2033
Joudaki, S., Blake, C., Johnson, A., et al. 2018, MNRAS, 474, 4894
Joudaki, S., Hildebrandt, H., Traykova, D., et al. 2020, A&A, 638, L1
Kaufman, G. 1967, Center for Operations Research and Econometrics, Catholic University of Louvain, Heverlee, Belgium, Report No. 6710
Khoury, J., & Weltman, A. 2004, Phys. Rev., D, 69, 044026
Kitaura, F.-S., Rodríguez-Torres, S., Chuang, C.-H., et al. 2016, MNRAS, 456, 4156
Koyama, K. 2018, Int. J. Mod. Phys. D, 27, 1848001
Kuijken, K., Heymans, C., Dvornik, A., et al. 2019, A&A, 625, A2
Kunz, M., Trotta, R., & Parkinson, D. R. 2006, Phys. Rev. D, 74, 023503
Lattanzi, M., & Gerbino, M. 2018, Front. Phys., 5, 70
Lawrence, E., Heitmann, K., Kwan, J., et al. 2017, ApJ, 847, 50
Lesgourgues, J., & Pastor, S. 2006, Phys. Rep., 429, 307
Lewis, A., & Challinor, A. 2006, Phys. Rep., 429, 1
Lewis, A., Challinor, A., & Lasenby, A. 2000, ApJ, 538, 473
Liddle, A. R. 2007, MNRAS, 377, L74
Liu, X., Li, B., Zhao, G. B., et al. 2016, Phys. Rev. Lett., 117, 051101
MacCrann, N., Zuntz, J., Bridle, S., Jain, B., & Becker, M. R. 2015, MNRAS, 451, 2877
McCarthy, I. G., Schaye, J., Bird, S., & Le Brun, A. M. C. 2017, MNRAS, 465, 2936
McElreath, R. 2015, Statistical Rethinking: A Bayesian Course with Examples in R and Stan (Boca Raton: CRC Press LLC)
Mead, A. J. 2017, MNRAS, 464, 1282
Mead, A. J., Heymans, C., Lombriser, L., et al. 2016, MNRAS, 459, 1468
Mead, A. J., Brieden, S., Tröster, T., & Heymans, C. 2021, MNRAS, 502, 1401
Nelder, J. A., & Mead, R. 1965, Comput. J., 7, 308
Oliphant, T. E. 2006, A Guide to NumPy (USA: Trelgol Publishing), 1
Ooba, J., Ratra, B., & Sugiyama, N. 2018, ApJ, 864, 80
Park, C.-G., & Ratra, B. 2019, ApJ, 882, 158
Park, C.-G., & Ratra, B. 2020, Phys. Rev., D, 101, 083508
Planck Collaboration XIII. 2016, A&A, 594, A13
Planck Collaboration XIV. 2016, A&A, 594, A14
Planck Collaboration VI. 2020, A&A, 641, A6
Planck Collaboration VIII. 2020, A&A, 641, A8
Pontecorvo, B. 1958, Sov. J. Exp. Theor. Phys., 6, 429
Raveri, M., & Hu, W. 2019, Phys. Rev., D, 99, 043506
Riess, A. G., Casertano, S., Yuan, W., Macri, L. M., & Scolnic, D. 2019, ApJ, 876, 85
Ross, A. J., Beutler, F., Chuang, C.-H., et al. 2017, MNRAS, 464, 1168
Sakstein, J. 2018, Int. J. Mod. Phys. D, 27, 1848008
Sánchez, A. G. 2020, Phys. Rev., D, 102, 123511
Sánchez, A. G., Scoccimarro, R., Crocce, M., et al. 2017, MNRAS, 464, 1640
Schmidt, F., Lima, M., Oyaizu, H., & Hu, W. 2009, Phys. Rev., D, 79, 083518
Schneider, P., van Waerbeke, L., Kilbinger, M., & Mellier, Y. 2002, A&A, 396, 1
Scolnic, D. M., Jones, D. O., Rest, A., et al. 2018, ApJ, 859, 101
Skilling, J. 2006, Bayesian Anal., 1, 833
Spiegelhalter, D. J., Best, N. G., Carlin, B. P., & Van Der Linde, A. 2002, J. R. Stat. Soc.: Ser. B (Stat. Meth.), 64, 583
Spurio Mancini, A., Köhlinger, F., Joachimi, B., et al. 2019, MNRAS, 490, 2155
Torrado, J., & Lewis, A. 2020, ArXiv e-prints [arXiv:2005.05290]
Tröster, T., Sánchez, A. G., Asgari, M., et al. 2020, A&A, 633, L10
Trotta, R. 2008, Contemp. Phys., 49, 71
Troxel, M. A., MacCrann, N., Zuntz, J., et al. 2018, Phys. Rev., D, 98, 043528
van den Busch, J. L., Hildebrandt, H., Wright, A. H., et al. 2020, A&A, 642, A200
Vehtari, A., Gelman, A., & Gabry, J. 2017, Stat. Comput., 27, 1413
Wang, D. 2020, ArXiv e-prints [arXiv:2008.03966]
Watanabe, S., & Opper, M. 2010, J. Mach. Learn. Res., 11
Will, C. M. 2014, Liv. Rev. Rel., 17, 4
Wong, K. C., Suyu, S. H., Chen, G. C. F., et al. 2020, MNRAS, 498, 1420
Wright, A. H., Hildebrandt, H., Kuijken, K., et al. 2019, A&A, 632, A34
Wright, A. H., Hildebrandt, H., van den Busch, J. L., & Heymans, C. 2020, A&A, 637, A100
Yao, Y., Vehtari, A., Simpson, D., & Gelman, A. 2018, Bayesian Anal., 13, 917
Zuntz, J., Paterno, M., Jennings, E., et al. 2015, Astron. Comput., 12, 45

Appendix A: Baryonic effects

Asgari et al. (2021) and Heymans et al. (2021) used the model of Mead et al. (2016), HMCODE, to predict the non-linear matter power spectrum and marginalise over the effect of baryons. The effect of baryons in HMCODE is modelled by a phenomenological 'bloating' of the dark-matter halos and changing the halo concentration. Recently, Mead et al. (2021) proposed a new, physically motivated modelling approach within the HMCODE-framework, which provides a parameterisation of the effect of feedback from active galactic nuclei (AGN) on the matter power spectrum. To test whether this new parameterisation affects our cosmology constraints, we vary the parameter $\log_{10}\left(\frac{T_{\rm AGN}}{\rm K}\right)$ over the range $[7.3, 8.3]$, a conservative choice as it extends well beyond the range $7.6 < \log_{10}\left(\frac{T_{\rm AGN}}{\rm K}\right) < 8.0$ found to reproduce observations in the BAHAMAS suite of hydrodynamical simulations (McCarthy et al. 2017). Higher values of $\log_{10}\left(\frac{T_{\rm AGN}}{\rm K}\right)$ correspond to more violent feedback, which expels more gas from halos, thus lowering the power on intermediate scales.

The resulting parameter constraints are presented in Fig. A.1. We find good agreement with the result based on the previous version of HMCODE (Mead et al. 2016). The preference for low values of $\log_{10}\left(\frac{T_{\rm AGN}}{\rm K}\right)$ is consistent with the preference for high values of $A_{\rm bary}$ in the KiDS-1000 cosmic shear and 3×2 pt data. We caution against a too literal interpretation of this parameter, as other effects can mimic the suppression of the matter power spectrum at intermediate to small scales.

Unlike the purely phenomenological modelling of the effect of baryonic processes in HMCODE, the model in HMCODE-2020 is more physically motivated, including gas and stellar components. As such, it does not have a dark matter-only limit, as diffuse gas always causes a degree of suppression of power at intermediate scales and stars cause an increase of power at the smallest scales. Furthermore, the suppression of power due to AGN feedback sets in at larger scales, with the strongest feedback scenario considered here, $\log_{10}\left(\frac{T_{\rm AGN}}{\rm K}\right) = 8.3$, exhibiting a stronger suppression of the matter power spectrum for $k \lesssim 10\,h^{-1}$ Mpc than the strongest feedback scenario considered in the fiducial analysis, $A_{\rm bary} = 2$. This model-inherent suppression of power serves to exclude low values of S_8, while the freedom of the model to predict a strong suppression due to our wide prior on $\log_{10}\left(\frac{T_{\rm AGN}}{\rm K}\right)$ allows for high values of S_8. Together, these effects cause a shift of the marginal S_8 posterior to slightly larger values, reducing the tension of our cosmic shear results with *Planck* from $2.8-3.2\sigma$ in the fiducial case to $2.3-2.5\sigma$ when using HMCODE-2020. This better agreement in S_8 is partially driven by the stronger correlation between $\Omega_{\rm m}$ and S_8 in the case of the HMCODE-2020 model. Using $\Sigma_8 = \sigma_8\,(\Omega_{\rm m}/0.3)^{0.58}$ instead, which provides a better description of the degeneracy direction in $\Omega_{\rm m}$ and σ_8 (Asgari et al. 2021), reduces the tension from $3.2-3.4\sigma$ to 2.9σ. The effect on the 3×2 pt results is smaller, reducing the tension from 3.1σ to 2.9σ. The shift of the 3×2 pt best-fit value of S_8 in terms of the S_8 uncertainty when using the HMCODE-2020 model is 0.26σ, similar to the shift observed when using HALOFIT instead of HMCODE (Joachimi et al. 2021). This result therefore confirms the conclusions of Joachimi et al. (2021): the uncertainty in the non-linear matter power spectrum prescription is currently one of the dominant systematics in the modelling and cosmology inference for KiDS.

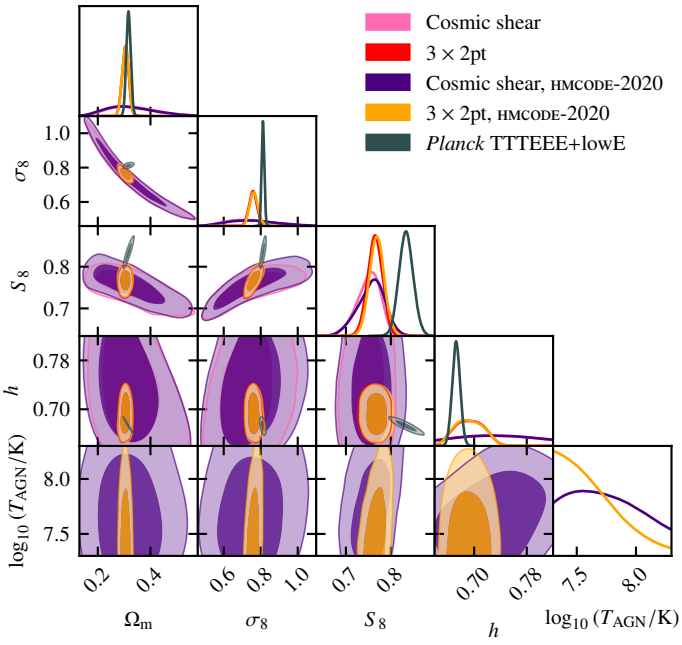

Fig. A.1. Comparison of the KiDS-1000 cosmic shear and 3×2 pt parameter constraints for different choices of the non-linear modelling of the matter power spectrum. The pink (cosmic shear) and red (3×2 pt) contours are derived using our fiducial setup, using the Mead et al. (2016) HMCODE model. The purple (cosmic shear) and orange (3×2 pt) contours use the updated Mead et al. (2021) model with a physically motivated modelling of baryonic effects. The *Planck* TTTEEE+lowE contours are shown in grey.

Appendix B: Extended data cuts and prior choices

Tröster et al. (2020) and Heymans et al. (2021) found a preference for low values of the spectral index $n_{\rm s}$ inferred from the clustering and 3×2 pt analyses. It was speculated that large-scale systematics in the galaxy clustering measurement (for BOSS DR12, see Ross et al. 2017) could be responsible but they argued that the main cosmological results, namely constraints on S_8, are not affected. Here we explore this preference for low values of $n_{\rm s}$ further by exploring the effect of data cuts that discard the large-scale information in the clustering measurements, as well as the effect of fixing $n_{\rm s}$, on the remaining cosmological parameters.

The resulting constraints are shown in Fig. B.1. Excising large-scale galaxy clustering data from the 3×2 pt data vector by limiting the maximum separation in the correlation function wedges to $s_{\rm max} = 100\,h^{-1}$ Mpc or $s_{\rm max} = 75\,h^{-1}$ Mpc primarily degrades the constraining power in $\Omega_{\rm m}$ as a consequence of removing the information about the BAO peak. These scale cuts only cause small changes in other parameters and leave S_8 unchanged.

In a similar vein, fixing $n_{\rm s}$ breaks its degeneracies with $\Omega_{\rm m}$ and σ_8, resulting in slightly tighter constraints on these parameters but leaving S_8 unaffected. We thus conclude that our analysis is robust to these systematics.

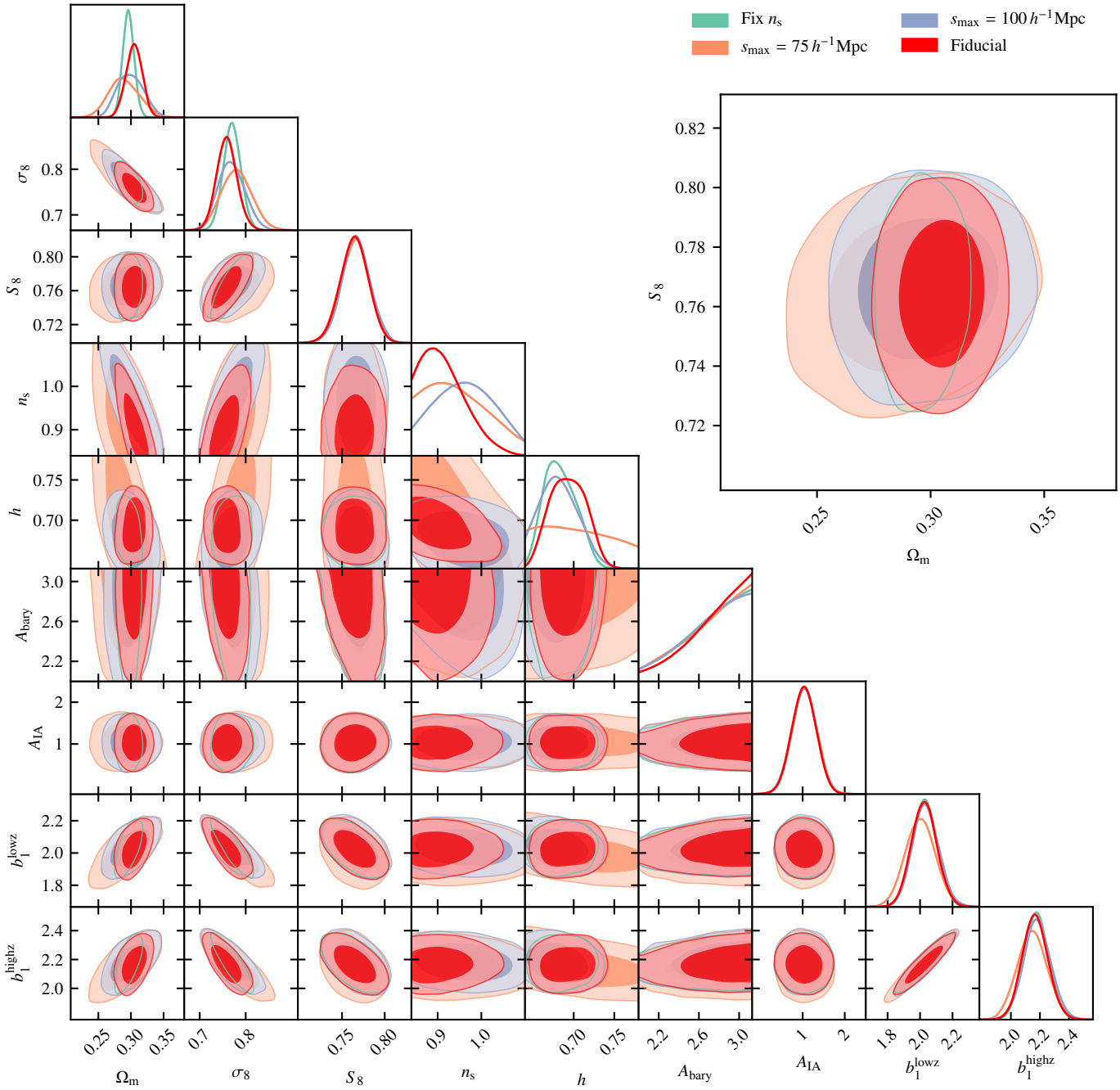

Fig. B.1. Effect of fixing n_s and discarding galaxy clustering data at large scales. Constraints when n_s is fixed are shown in turquoise, while those were the maximum separation s_{max} in the correlation function wedges is limited are shown in blue ($s_{max} = 100\,h^{-1}$ Mpc) and orange ($s_{max} = 75\,h^{-1}$ Mpc), compared to the fiducial setup in red.